

Dual-Conductive and Stiffness-Morphing Microneedle Patch Enables Continuous In Planta Monitoring of Electrophysiological Signal and Ion Fluctuation

Lingxuan Kong, Hanqi Wen, Yifei Luo, Xiaodong Chen, Xing Sheng, Yuxin Liu,* and Peng Chen*



Cite This: *ACS Appl. Mater. Interfaces* 2023, 15, 43515–43523



Read Online

ACCESS |

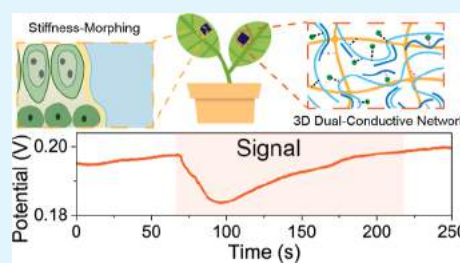
Metrics & More

Article Recommendations

Supporting Information

ABSTRACT: The use of conductive microneedles presents a promising solution for achieving high-fidelity electrophysiological recordings with minimal impact on the interfaced tissue. However, a conventional metal-based microneedle suffers from high electrochemical impedance and mechanical mismatch. In this paper, we report a dual-conductive (i.e., both ionic and electronic conductive) and stiffness-morphing microneedle patch (DSMNP) for high-fidelity electrophysiological recordings with reduced tissue damage. The polymeric network of the DSMNP facilitates electrolyte absorption and therefore allows the transition of stiffness from 6.82 to 0.5139 N m⁻¹. Furthermore, the nanoporous conductive polymer increases the specific electrochemical surface area after tissue penetration, resulting in an ultralow specific impedance of 893.13 Ω mm² at 100 Hz. DSMNPs detect variation potential and action potential in real time and cation fluctuations in plants in response to environmental stimuli. After swelling, DSMNPs mechanically “lock” into biological tissues and prevent motion artifact by providing a stable interface. These results demonstrate the potential of DSMNPs for various applications in the field of plant physiology research and smart agriculture.

KEYWORDS: *conducting polymers, microneedle, plant physiology, smart agriculture, in situ biosensors*



INTRODUCTION

The study of plant physiology has traditionally been hindered by molecular and cellular biology techniques that provide limited insights into dynamic biological processes and require destructive sampling methods. To address this issue, the development of bioelectronic interfaces that allow real-time monitoring of plant physiology is crucial for both fundamental research and practical applications in agriculture. Microneedle patches have garnered significant attention due to its minimally invasive nature.^{1–6} In recent years, conducting metallic microneedle patches have been explored for the detection of biopotentials and biomarkers in skin interstitial fluid.^{7–9} However, these patches face challenges such as substantial mechanical mismatch between metallic materials and biological tissues and high impedance due to electrochemical reactions at the metal–fluid interface, leading to high noise recording and motion artifacts.¹⁰ Conducting polymers, such as poly(3,4-ethylenedioxythiophene) polystyrene sulfonate (PEDOT:PSS), have emerged as promising alternatives due to their biocompatibility, dual electronic–ionic conductivity, and mechanical compatibility.^{11–13} While conducting polymer-based microneedle patches have been demonstrated, they lack mechanical strength for successful penetration into biological tissues. For example, hyaluronic acid, a typical material choice for microneedles¹⁴ is unable to form a percolating conductive pathway without sacrificing its mechanical strength.

In this study, we report the first dual-conductive stiffness-morphing microneedle patches (DSMNPs) using PEDOT:PSS and poly(lactic-co-glycolic acid) (PLGA). Our DSMNPs offer a low-impedance bioelectronic interface and good mechanical strength compared to a conventional metal electrode. In addition, by utilizing PLGA's thermoplasticity, our DSMNPs can be fabricated through a simple thermo-pressing method, making it amenable for low-cost large-scale production. As proof-of-concept demonstrations, we applied our DSMNPs for real-time in situ detection of electrophysiological signals and cation concentrations in response to environmental stimuli.

RESULTS AND DISCUSSION

Fabrication of DSMNP. Conducting polymer-based electrode allows for capturing both electrical and ionic signals due to its dual-conductivity (Figure 1a). However, pristine conducting polymer PEDOT:PSS lacks the sufficient mechanical strength to penetrate biological tissues. We address this challenge by blending biocompatible poly lactic-co-glycolic acid

Received: June 18, 2023

Accepted: August 23, 2023

Published: September 7, 2023



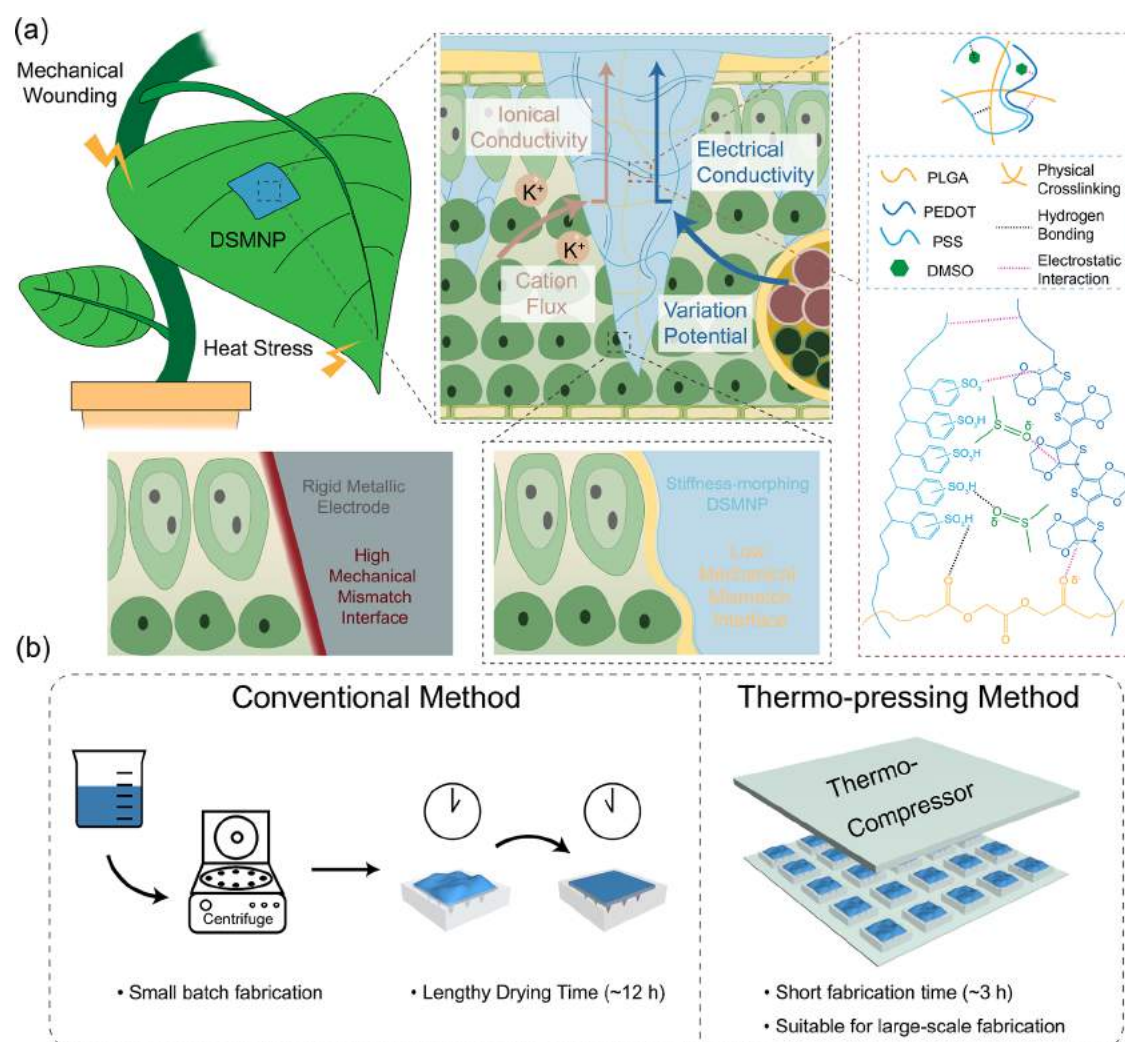


Figure 1. Polymeric DSMNP detects stress-induced variation potential and ion fluctuation by providing a low-mechanical-mismatch interface, which can be manufactured by a large-scale thermo-pressing method. Schematic illustration of (a) plant electrophysiology and ion flux monitoring by DSMNP and (b) comparison between conventional and thermo-pressing microneedle fabrication method.

(PLGA) into the PEDOT:PSS matrix. PLGA with rich carboxyl groups noncovalently cross-link with PEDOT:PSS via the electrostatic interaction with the PEDOT chains and hydrogen bonding with the PSS chains (Figure 1a). As a result, the mechanical property of the PEDOT:PSS matrix is substantially improved. In addition, dimethyl sulfoxide (DMSO) was used not only as the solvent for both PLGA and PEDOT:PSS but also as the secondary dopant of PEDOT and H-bond acceptor of PSS, whereby promoting the formation of a conductive network.¹⁵ DSMNP performs a stiffness-morphing property after electrolyte adsorption, forming a low-mechanical-mismatch interface with plant tissue compared to the rigid metallic electrode (Figure 1a). The viscous PEDOT:PSS/PLGA mixture was poured on the polydimethylsiloxane (PDMS) mold and immersed in ethanol to extract excess DMSO, followed by solvent evaporation by heating. The thermoplasticity property of PLGA allows thermo-pressing PEDOT:PSS/PLGA polymer mixture into the PDMS mold to form DSMNPs as illustrated in Figure S1. Compared to the conventional microneedle fabrication methods that require centrifugation and lengthy drying time, the demonstrated thermo-pressing approach is amenable for low-cost large-scale production (Figure 1b).

Characterizations of DSMNP. As shown by optical and scanning electron microscopy (SEM), DSMNP consists of an array of 3×3 pyramidal microneedles with the tip size of $\sim 10 \mu\text{m}$, length of $500 \mu\text{m}$, base dimension of $250 \mu\text{m}$, and inter-MN spacing of $400 \mu\text{m}$ (Figures 2a and S2). With the increase of the weight ratio of PEDOT:PSS, the mechanical strength of DSMNP decreases (Figure 2b), whereas its conductivity increases (Figure 2c). Despite the highest conductivity, DSMNP with 30 wt % loading of PEDOT:PSS is unable to perform tissue penetration. DSMNP with 20 wt % PEDOT:PSS offers relatively good conductivity (3.19 S/cm) with a cell constant of 40.192 cm^{-1} (Table S1) but gives much higher stiffness (providing a force of 3.5 N/needle to ensure easy tissue penetration, at 0.5 mm displacement without breaking) than that with 25 and 30 wt % PEDOT:PSS loading. Therefore, this optimal ratio was chosen to make DSMNPs for the subsequent experiments. To further investigate the electrical property of DSMNP, its electrical spectra impedance was obtained (Figure S3). Nyquist and Bode plots presented low impedance of DSMNP and phase angle change demonstrated its dual conductivity, and by fitting the Randles circuit, we showed DSMNP low resistance of $3.203 \Omega \text{ cm}^2$ and a high capacitance of $4.484 \times 10^{-3} \text{ S s}^{-1} \text{ cm}^{-2}$ (Table S2). The

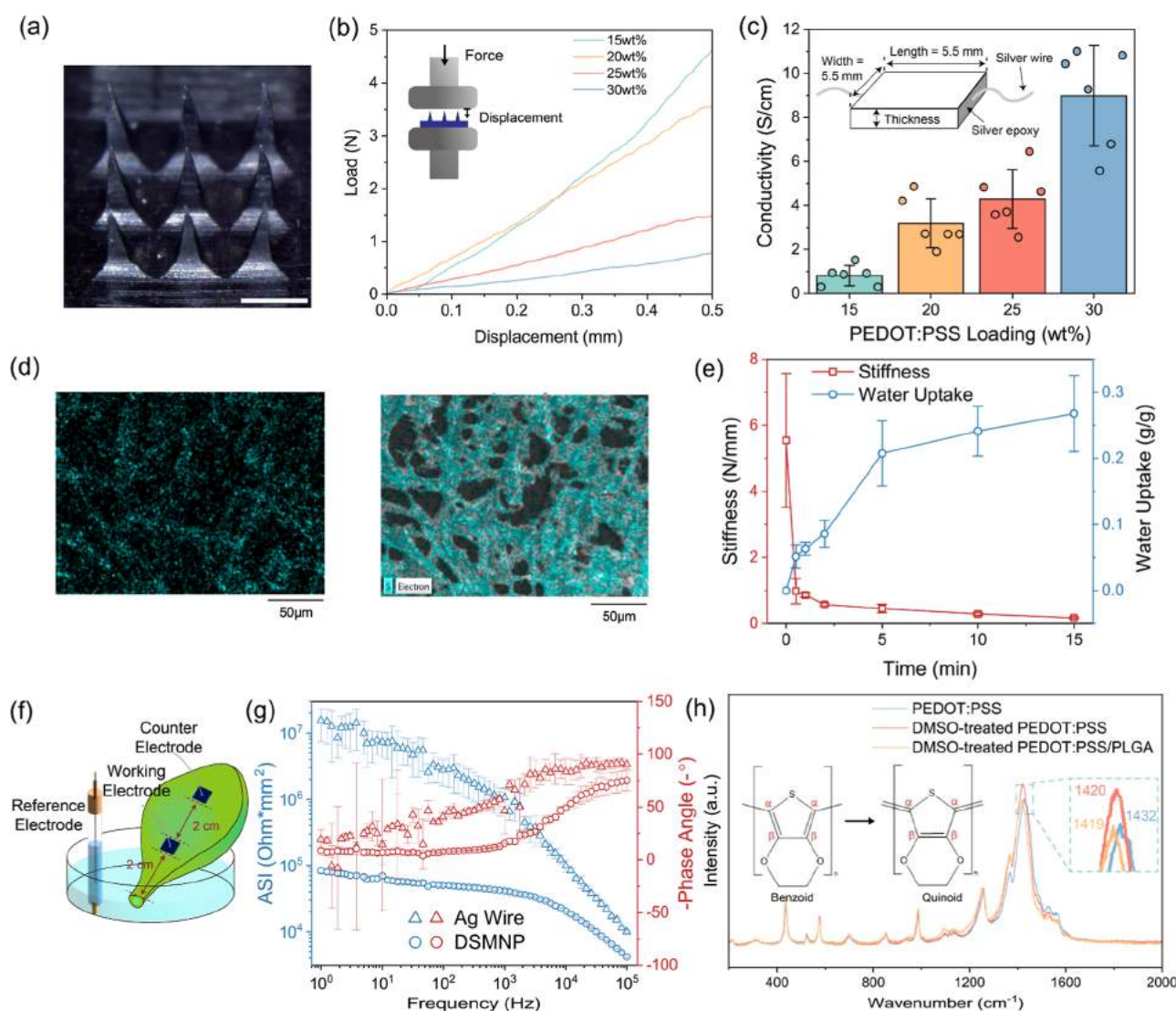


Figure 2. Electrical and mechanical characterizations of DSMNP. (a) Optical image of DSMNP. Scale bar: 500 μm. (b) Mechanical compression test of DSMNPs with different PEDOT:PSS loadings. Inset: illustration of the experimental setup. (c) Conductivity of DSMNPs with different PEDOT:PSS loadings. $n = 6$. Inset: illustration of the experiment setup for conductivity measurement. (d) EDX mapping of sulfur in PLGA/PEDOT:PSS composite (left) and its merge with SEM image (right). (e) Stiffness and water uptake change of DSMNPs with penetration into agarose gel. $n = 3$. (f) Experimental setup of the EIS measurement. (g) Area-specific impedance spectra (left) and phase angle (right) of Ag wire- and DSMNP-leaf interface. (h) Raman spectra of PEDOT:PSS, DMSO-treated PEDOT:PSS, and DMSO-treated PEDOT:PSS/PLGA. Inset: change of PEDOT chain after DMSO treatment.

combination of strong mechanical property and high conductivity is endowed by interpenetrating the PEDOT:PSS and PLGA network.

As shown by energy-dispersive X-ray (EDX) analysis result, EDX mapping and its SEM image (Figures 2d and S4), a phase separation between high sulfur density region and low sulfur density region can be observed, which is inferred to be PEDOT:PSS-rich region and PLGA-rich region, respectively. Different from the pristine PLGA microneedle, DSMNP can absorb electrolyte, and therefore the stiffness of the microneedle decreases substantially. The stiffness of DSMNP decreases from 5.54 to 0.17 N mm⁻¹ by adsorbing 0.27 g g⁻¹ electrolyte at 15 min after penetration (Figures 2e and S5). After stiffness-morphing, the soft polymeric network of DSMNP could maintain conformal contact with the plant tissue, therefore allowing high-fidelity electrophysiological recording with reduced motion artifact (Figure S6).¹⁶ When

there is mechanical disturbance such as wind, smaller mechanical mismatch between DSMNP and plant tissue ensured chronic interface stability and caused less damage compared to the rigid metal electrode.¹⁷ Moreover, the thin microneedle patch allows a bending angle up to 30° while resistance variation change is below 5% (Figure S7).

Using freshly detached *Epipremnum aureum* leaf as the in vitro model, we tested the electrochemical impedance of DSMNP and compared that with a silver wire (Figure 2f,g). The latter is commonly used as an electrode to record electrophysiological signals in plants.¹⁸ Impedance spectra showed that area specific impedance of a DSMNP-leaf interface is substantially lower than that of a silver wire-leaf interface from 1 to 100,000 Hz (e.g., 893.13 vs 5478.24 Ω mm² at 100 Hz). The low impedance may be contributed by the dual conductivity and nanoporosity of PEDOT:PSS.¹⁹ By fitted into Randles circuit model, DSMNP shows significantly

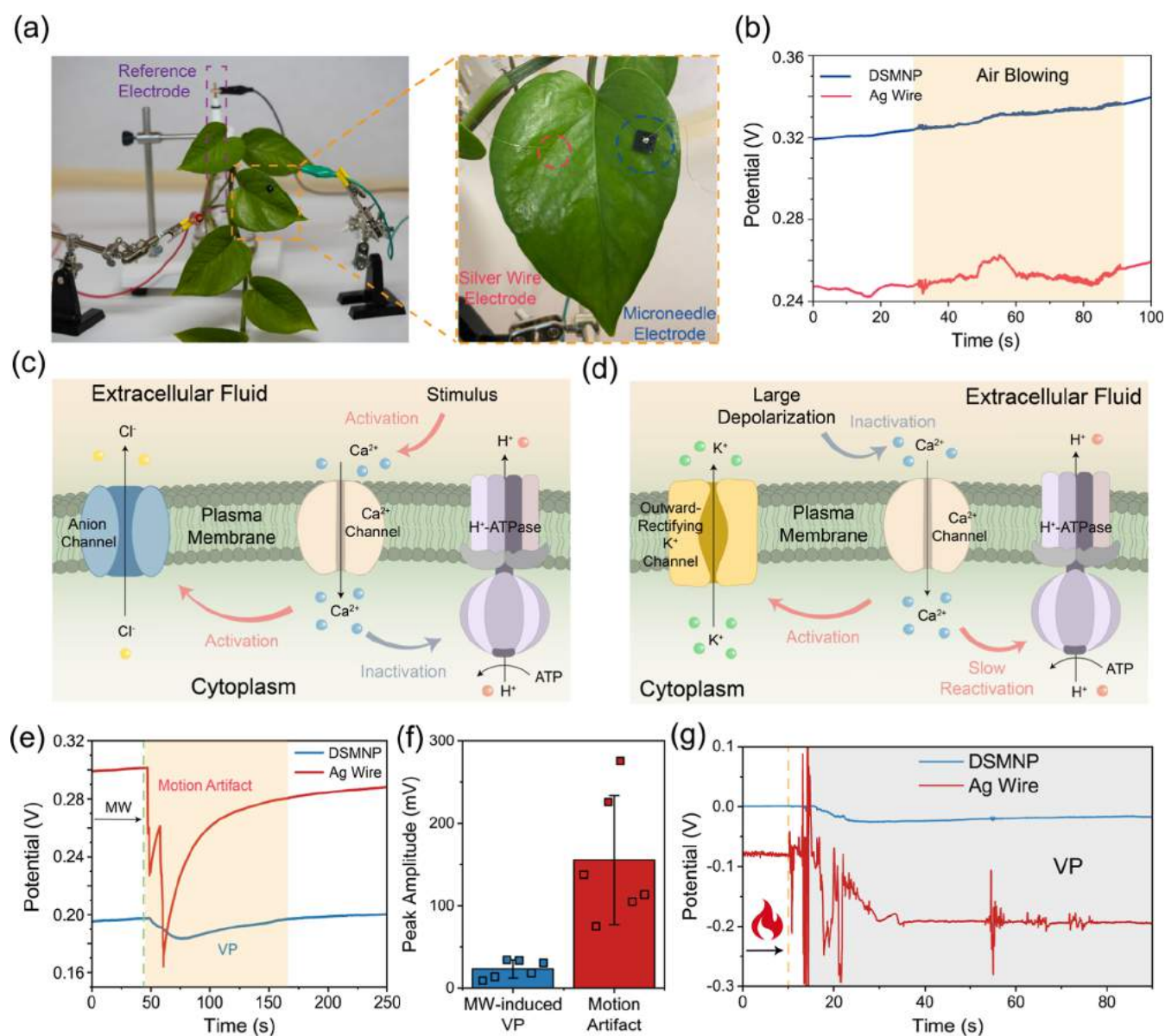


Figure 3. Recording of electrophysiological signals in *Epipremnum aureum*. (a) Experimental setup. (b) Recorded biopotentials by DSMNP and Ag wire electrodes in the presence of air blowing to mimic wind disturbance. (c) Scheme of depolarization of VP. (d) Scheme of repolarization of VP. (e) MW-induced electrophysiological response monitored by DSMNP and Ag wire. (f) Peak amplitude comparison between MW-induced VP and motion artifact. (g) Flame-induced electrophysiology response monitored by the DSMNP and Ag wire.

lower charge transfer resistance (1.245×10^4 vs $7.776 \times 10^5 \Omega \text{ mm}^{-2}$) and high double-layer capacitance (3.945×10^{-9} vs $3.175 \times 10^{-10} \text{ S s}'' \text{ mm}^2$) than silver wire (Figure S8 and Table S3). This can be explained by the high specific electrochemical surface area of DSMNP's three-dimensional polymeric network after electrolyte absorption. In vitro experiment on agarose gel (covered with water-impermeable parafilm) also demonstrated low impedance of DSMNP-leaf interface compared to Ag wire-leaf interface (3337.47 vs $37978.69 \Omega \text{ mm}^2$ at 100 Hz , Figure S9), and well-fitted Randles model showed low charge transfer resistance (9.697×10^5 vs $1.161 \times 10^9 \Omega \text{ mm}^2$) and high double layer capacitance (5.791×10^{-3} vs $2.256 \times 10^{-5} \text{ S s}'' \text{ mm}^{-2}$) (Table S4).

Figure 2h shows the Raman spectra of pristine PEDOT:PSS, DMSO-treated PEDOT:PSS, and DMSO-treated PEDOT:PSS/PLGA mixture. For PEDOT:PSS, the peak at 1432 cm^{-1} is originated from $C_\alpha=C_\beta$ stretching of the

thiophene ring on PEDOT.²⁰ With the DMSO treatment, this peak redshifts to 1420 cm^{-1} , suggesting that PEDOT chains change from the benzoid structure (a core-shell conformation) to quinoid structure (an extended coil conformation).²¹ This may be attributed to PEDOT-DMSO and PSS-DMSO interactions which disrupt electrostatic attraction between PEDOT chains and PSS chains, resulting in stretching of PEDOT chains and phase separation of PEDOT:PSS. Formation of PSS-DMSO hydrogen bonding can screen the negatively charged sulfonic acid groups of PSS, thus promoting self-aggregation of PEDOT.¹⁵ A denser packing of PEDOT chains largely decreases the energy barrier of charge hopping within the conductive network, leading to conductivity enhancement.²² The addition of PLGA causes no obvious shift of the Raman peak (1419 cm^{-1}), indicating that it does not interfere with the arrangement of PEDOT chains. Fourier-transform infrared (FTIR) spectra of pristine PEDOT:PSS and

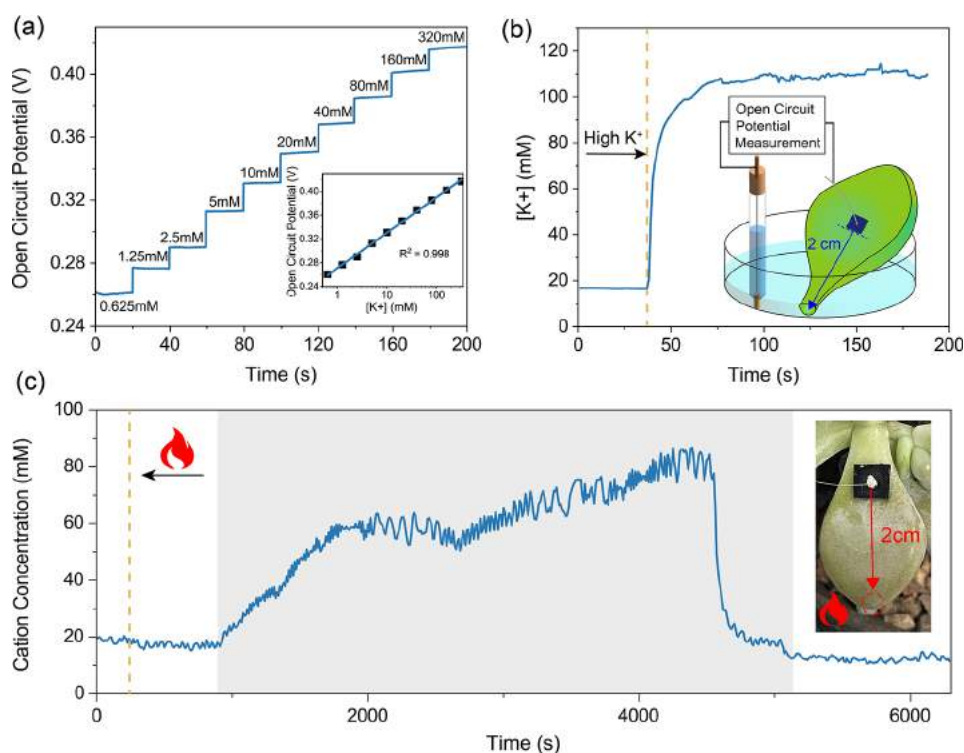


Figure 4. Monitoring cation concentration in *Graptopetalum paraguayense* using a cation-sensitive DSMNP. (a) Open circuit potential of a DSMNP in response to stepwise increase of KCl concentration. Inset: open circuit potential vs logarithm of K^+ concentration. (b) Increase of cation concentration in a fresh leaf due to diffusion. (c) In vivo real-time monitoring of cation variation in response to flame-burn. Inset shows the experimental setup.

DMSO-doped PEDOT:PSS showed that peaks related to C_{α} -S bond perturbations on thiophene ring of PEDOT (at 832 and 976 cm^{-1}) are blue-shifted to 815 and 948 cm^{-1} , respectively (Figure S10).²³ This can be explained by the dipole moment increase of PEDOT induced by weaker electrostatic interaction with a long PSS chain.

In Planta Electrophysiological Monitoring. As a proof-of-concept demonstration, we first investigated the ability of DSMNP to detect electrophysiological signals from an aquatic landscape plant, *E. aureum*, and compared it with the conventional silver wire electrode for plant electrophysiology. The plant and the Ag/AgCl reference electrode were placed in phosphate-buffered saline (PBS) solution. A DSMNP electrode was pressed onto a leaf (1 cm from the midrib), while a silver wire electrode was threaded through symmetrically on the other side of the midrib for simultaneous recording of biopotential (Figure 3a). To test the electrode stability, rapid air flow was used to simulate the wind in the field. As shown in Figure 3b, the baseline of the biopotential recording from the silver wire fluctuates dramatically under windy conditions, with a root-mean-square (RMS) of 3.69 mV (after baseline correction), which is much higher than that of the DSMNP electrode (0.78 mV, after baseline correction) (Figure S11). The peak-to-peak fluctuation is ~ 18.23 mV, which shadows variation potentials (VP) in plants in response to some stimuli, such as mechanical wounding (MW) (15–40 mV),²⁴ thus preventing silver wire electrode from high-fidelity and reliable recording. The good stability of DSMNP can be explained by intimate interface between microneedles and plant tissues and low Young's modulus mismatch between hydrated PEDOT:PSS/PLGA composite (~ 3.4 MPa) and plant tissue (1–10 MPa).²⁵ Moreover, slight swelling of microneedles

upon adsorption of sap helps to mechanically “lock” them in position and form a robust electrically continuous interface between ion-conducting biofluid and polymer matrix with dual ionic and electronic conductivity.

Plants produce electrophysiological signals in response to the environmental stimuli, which in turn trigger cascaded physiological events, such as modulation of gene expression and phytohormone level.^{26,27} Monitoring the electrophysiological signals from the plants is instrumental to detect environmental stress for smart agriculture and understand plant physiology. In response to MW (e.g., insect bite), VP will be generated and propagated to elicit stress responses.²⁸ VP, also called slow-wave potential, is initiated by opening of Ca^{2+} channels (allowing influx of Ca^{2+} ions) and Ca^{2+} influx thereby activates the calcium-dependent anion channel (allowing efflux of Cl^- ions) and inactivates the H^+ -ATPase to depolarize the cell membrane (Figure 3c).²⁹ Subsequently, large depolarization inactivates the Ca^{2+} -channel, and membrane repolarizes because of the activation of K^+ channels (allowing efflux of K^+ ions) triggered by decreased cytoplasmic Ca^{2+} concentration (Figure 3d).²⁷ Different from action potential (AP), the membrane repolarization is greatly prolonged owing to slow reactivation of H^+ -ATPase (Figure 3d).³⁰ When a small MW was induced by a clamp at the leaf tip, an instantaneous response was recorded from the silver wire electrode, which was much faster and larger (155.53 vs 23.28 mV) than the expected VP (Figure 3e,f). Conceivably, this was an artificial electrical signal due to mechanical disturbance at the high-mechanical-mismatch electrode-tissue interface, which buried the VP signal. In contrast, DSMNP showed stiffness-morphing transition after electrolyte adsorption, enabling the formation of a conformal, low-mechanical-mismatch electrode-tissue

interface. Thus, DSMNP was able to record a gradually developed VP with a prolonged repolarizing phase, which resembles the morphology and amplitude of those previously reported without significant motion artifact.²⁴ Activated by strong flame-burning stimulations to mimic extreme temperature changes, a large VP with fast depolarization and slow repolarization characteristics was successfully recorded by DSMNP (Figure 3g). The amplitude of flame-burn induced VP was much larger (79.30 vs 23.28 mV) and repolarizing tail was longer than that of mechanical wound-induced VP (Figure S12), and this can be explained that flame-burn is an intense stimulation that significantly suppresses the reactivation of H⁺-ATPase.³¹ Propagation speed (5.41–14.29 cm min⁻¹), depolarization duration (3.3–20.775 s), and repolarization duration (118–510.3 s) reported are consistent with previous research studies.^{24,32} However, we observed a large amount of electrical artifact when recorded by silver wire, which might be because of heat-induced leaf contraction and coiling. In contrast, DSMNP recorded stable plant electrophysiological signal during leaf deformation due to the soft and conformal interface post stiffness-morphing process.

In Planta Detection of Ion Fluctuation. Abnormal ion concentration is related to many plant diseases, such as fruit cracking and leaf burn,³³ and consumption of high-sodium agricultural products brings stress on the kidney and cardiovascular system.^{34,35} Variation of cation concentrations can be gradually induced by apoptosis of plant cells and salinity stress, or be instantaneously caused by wounding as cytosolic cations (mainly K⁺, 100–200 mM) flow into extracellular fluid.³⁶ Conventionally, the extracellular ion concentration is estimated by conductivity measurement after immersing chopped plant tissues in a solution, which is destructive and cannot provide real-time measurement.³⁷ Alternatively, a luminescence assay can be used. However, the bulky luminescence imaging system limits its application for in situ real time monitoring.³⁸

Cation-selective membrane (Nafion) was dip-coated onto its surface to enable a DSMNP with cation selectivity. As shown in Figure 4a, such a DSMNP can potentiometrically detect a wide range of K⁺ concentrations with a sensitivity of 59.25 mV per decade. Linear response retains even at the concentration as high as 320 mM. The nearly perfect Nernstian behavior (theoretical value of 59.16 mV/dec) is attributable to the low charge-transfer resistance and large specific capacitance of DSMNP owing to their dual conductivity as well as their three-dimensional interface with the electrolyte.

Graptopetalum paraguayense, a widely studied succulent plant,³⁹ was used as the model to test the cation-sensitive DSMNP. First, an ex situ experiment was performed to confirm the feasibility of using DSMNP to monitor the variation of ion concentration in real time (Figure 4b). Specifically, DSMNP was patched onto a leaf freshly detached from the plant and immersed in a low concentration KCl solution (1 mM). High concentration KCl solution (320 mM) was dropwise added until the final concentration reached 150 mM, which is much higher than the extracellular cation concentration in plants (typically <20 mM). The measured open-circuit potential was converted into cation concentration based on the calibration curve presented in Figure 4a. As shown in Figure 4b, the extracellular cation concentration increased from ~17 to ~110 mM with a time constant of ~6 s, resulting from ion diffusion through the plasmodesmata and extracellular matrix.

For in situ monitoring on live *G. paraguayense*, the reference Ag/AgCl electrode was inserted into the soil moistened by KCl solution (10 mM), and the working electrode (DSMNP) was applied 2 cm away from the tip of the tested leave. One-point-calibration was performed to determine the inherent potential offset between the calibration curve obtained in solution and the in situ measurement in soil.⁴⁰ As demonstrated in Figure 4c, a delayed gradual increase in extracellular cation concentration was recorded by DSMNP after a flame was briefly applied 2 cm away. Conceivably, this results from the burst release of intracellular K⁺ from the necrotic and apoptotic leaf cells into extracellular space and subsequent diffusion to the electrode site. The extracellular cation concentration reached ~85 mM, which, as expected, is slightly below the cytosolic K⁺ concentration (100–200 mM). Although the Nafion membrane is also permeable to Na⁺ and H⁺, K⁺ is the dominating cation in plants and flame-induced stress should not cause substantial change of Na⁺ and H⁺ concentrations.

CONCLUSIONS

The dual-conductive microneedle patches (DSMNPs) have both good conductivity to ensure high fidelity recording and good mechanical strength to ensure tissue penetration. Comparing to the conventional fabrication methods for microneedle patches, which require centrifugation and lengthy drying time, the herein demonstrated thermo-compressing method can be potentially automated without the need of centrifuge and amenable to low-cost large-scale production. DSMNPs detected electrophysiological signals (VP) and fluctuation of cation concentration in response to the environmental stimuli with lower noise level (0.780 vs 3.693 mV) compared with silver wires. The lightweight, biocompatibility, mechanical compatibility, dual electronic-ionic conductivity, and minimal invasiveness endow DSMNPs with the capability of real-time, long-term, and sensitive detection. Such new plant sensors are instrumental not only for fundamental studies but also for smart agriculturing. Using different ion-selective coatings, specific detection of Ca²⁺, K⁺, Na⁺, and Cl⁻ ions may be achieved. The development of DSMNPs represents a significant step forward in the field of bioelectronics, particularly in the realm of plant physiology. To date, the study of plant physiology relies primarily on molecular and cellular biology, which lacks real-time analysis capabilities and often involves destructive sampling. Our DSMNPs offer the potential for nondestructive real-time monitoring of plant physiology, which has significant implications for fundamental studies and smart agriculture.

EXPERIMENTAL SECTION

Materials. SYLGARD 184 Silicone Elastomer Kit was purchased from Dow Chemicals. Silver wire, PEDOT:PSS (dry pellet), DMSO, PLGA (858S), and Nafion perfluorinated resin solution (5 wt % in mixture of lower aliphatic alcohols and water), 2-hydroxyethyl methacrylate (HEMA), ethylene glycol dimethacrylate (EGDMA), ammonium persulfate (APS), and silver wire (diameter: 0.1 mm, 99.9% trace metals basis) were purchased from Sigma-Aldrich. Silver conductive epoxy adhesive (8330D) was purchased from MG Chemicals. All reagents were ACS grade and used without further purification. Metal microneedle positive molds were purchased from Micropoint Technologies. The Ag/AgCl reference electrode (R0201) was supplied by Tianjin Aida Hengsheng Technology Development Co., Ltd.

Fabrication of DSMNP. SYLGARD PDMS precursors and curing agent were mixed at a 10:1 weight ratio and stirred well before being

poured into the metal positive microneedle mold placed in a Petri dish. After degassing in a vacuum oven for 30 min, it was heated at 70 °C for 1 h to complete the curing process. Then, the negative PDMS mold was carefully detached from the Petri dish and heated at 70 °C overnight. Finally, the mold was cleaned by DI water sonication before use.

Subsequently, 20 w/v % of PLGA and 5 w/v % of PEDOT:PSS dry pellet were added to DMSO and stirred vigorously overnight to obtain a homogeneous and viscous solution. Then, it was poured onto PDMS negative mold and immersed in ethanol for 3 h to remove the excess DMSO. After heating at 80 °C for 30 min, a clay-like composite was obtained. It was then pressed into PDMS microneedle-shaped cavities by a thermocompressor operated at 100 °C with 10 KG compression force. Before being detached from the mold, the microneedle patch was cooled down at ambient temperature. Finally, silver epoxy was applied to join the microneedle patch and a silver wire, followed by curing at 75 °C for 10 min.

To endow DSMNP with selectivity for cations, we dip-coated microneedles in Nafion resin solution and dried at an ambient temperature. This process was repeated three times. To protect the Nafion layer during insertion, a layer of HEMA was coated due to its high toughness at the dry state and nonswelling property. Specifically, HEMA precursor solution was prepared by mixing HEMA (monomer, 200 mg mL⁻¹), APS (thermo-initiator, 20 mg mL⁻¹), and EGDMA (cross-linker, 2 mg mL⁻¹) into DI water for 1 h. Then, Nafion-coated microneedles were dip-coated in fresh prepared HEMA precursor solution and heated to polymerize (70 °C, 1 h).

Characterizations. DSMNPs were imaged by a Leica DVM6 microscope and a field-emission scanning electron microscope (JEOL JSM 6700F). FTIR spectra were recorded by a Nicolet iS50 FTIR Spectrometer. Raman spectra were recorded with a Renishaw inVia Reflex Raman spectrometer (laser wavelength 633 nm). Mechanical strength of microneedles was evaluated by an Instron 5543 Tensile Meter. Specifically, microneedle patch facing upward was placed on a stainless-steel plate while a compression force was applied vertically at the rate of 0.5 mm per minute. The displacement was measured until the maximum load (10 N) was reached.

The conductivity of DSMNP was evaluated by using an electrochemical workstation (CHI 760D, Chenhua). Silver wire was connected to the two edges of the DSMNP via silver epoxy adhesive (MG Chemicals), and the resistance across the microneedle patch was measured. The conductivity (σ) was calculated by the formula below: $\sigma = l/(R * w * d)$, where “ l ” is the length, “ R ” is the resistance, “ w ” is the width, and “ d ” is the thickness of DSMNP.

Electrophysiological signals were acquired by a USB-2610 Series DAQ (Smacq Technologies) with a sampling frequency of 100 Hz. Electrochemical impedance spectroscopy (EIS) was obtained by an electrochemical workstation (CHI 760D, Chenhua) in the frequency range of 1–100,000 Hz. EIS of DSMNP and of the electrode-agarose interface was obtained under a two-electrode configuration, and EIS of the electrode-leaf interface was obtained under a three-electrode configuration.

In Planta Monitoring of Electrophysiological Signals. Before the experiment, studied *E. aureum* was prepared by being bred in PBS for 2 weeks before experiments. The plant and Ag/AgCl reference electrode were placed in PBS, while DSMNP or silver wire electrode was mounted at 1 cm away from the midrib of the stimuli-applied leaf. Plant and electrodes were placed at the experiment site for 1 day without external disturbance before the experiment started. Electrophysiological signals were acquired by a USB-2610 Series DAQ (Smacq Technologies) with the sampling frequency of 100 Hz.

Rapid air flow generated by an industrial air blower was to mimic the strong wind in the field. MW was produced by pressing the leaf tip for 2 s using two PTFE molds with wavy-grained surface. Flaming wounding was created by burning at the leaf tip for 1 s using a subminiature industrial flame projector.

In Planta Monitoring of Ion Fluctuation. Change of the open circuit potential in response to the K⁺ concentration was calibrated in KCl solutions. Specifically, when the concentration of K⁺ increased,

open circuit potential was only recorded after intra- and extra-DSMNP K⁺ concentration reached equilibrium.

Ex situ ion fluctuation monitoring was performed on freshly detached *G. paraguayense* leaf. Specifically, DSMNP was patched at 2 cm away from the leaf tip, and the root of the leaf was immersed in a low concentration KCl solution (1 mM). High concentration KCl solution (320 mM) was dropwise added until the final concentration reached 150 mM. The measured open-circuit potential was converted into cation concentration based on the calibration curve.

G. paraguayense for experiments was bought from a local market and would be bred for 2 weeks. Before in situ monitoring on live *G. paraguayense*, one-point calibration was performed to determine the inherent potential offset between the calibration curve obtained in solution and the in situ measurement in soil. Briefly, the Ag/AgCl reference electrode was placed in soil that was fully moisture by 10 mM KCl solution and DSMNP was mounted at 2 cm away from leaf tip. Open circuit potential between reference electrode and DSMNP was compared with calibrated value and calibration line was shifted by this difference.

In situ ion fluctuation monitoring was performed immediately after one-point calibration. Specific tissue necrosis and cell apoptosis was induced by 5 s continuous flame burning using subminiature industrial flame projector, and open circuit potential was recorded until no fluctuation was observed.

■ ASSOCIATED CONTENT

SI Supporting Information

The Supporting Information is available free of charge at <https://pubs.acs.org/doi/10.1021/acsami.3c08783>.

Illustration of DSMNP fabrication; SEM image of DSMNP; EIS of DSMNP; EDS analysis of DSMNP; mechanical compression test of DSMNP before and after penetration; area-specific impedance (at 10 Hz) of DSMNP change after penetration; resistant variation when different bending angles are applied; EIS fitting of DSMNP- and Ag wire-leaf interface; EIS of DSMNP- and Ag wire-agarose interface with model fitting; FTIR spectra of pristine PEDOT:PSS and DMSO-doped PEDOT:PSS; wind-induced motion artifact RMS of DSMNP and Ag wire; comparison of VPs induced by flame-burning and MW; cell constants for DSMNP conductivity calculation; EIS fitting parameters of DSMNP; EIS fitting parameters of DSMNP- and Ag wire-leaf interfaces; and EIS fitting parameters of DSMNP- and Ag wire-agarose interfaces (PDF)

■ AUTHOR INFORMATION

Corresponding Authors

Yuxin Liu – Institute of Materials Research and Engineering (IMRE), Agency for Science, Technology and Research (A*STAR), Singapore 138634, Singapore; Department of Biomedical Engineering, College of Design and Engineering, 4 Engineering Drive 3, National University of Singapore, Singapore 117583, Singapore; Institute for Health Innovation & Technology/Healthtech, National University of Singapore, Singapore 117599, Singapore; The N.I Institute for Health, National University of Singapore, Singapore 117456, Singapore; orcid.org/0000-0003-0623-9402; Phone: +65 65660182; Email: lyx@nus.edu.sg

Peng Chen – School of Chemistry, Chemical Engineering and Biotechnology, Nanyang Technological University, Singapore 637457, Singapore; Institute for Digital Molecular Analytics and Science (IDMxS), Nanyang Technological University,

Singapore 636921, Singapore; Phone: +65 65141086;
Email: ChenPeng@ntu.edu.sg

Authors

Lingxuan Kong – School of Chemistry, Chemical Engineering and Biotechnology, Nanyang Technological University, Singapore 637457, Singapore

Hanqi Wen – School of Chemistry, Chemical Engineering and Biotechnology, Nanyang Technological University, Singapore 637457, Singapore; Institute of Flexible Electronics Technology of THU, Jiaxing, Zhejiang 314000, China

Yifei Luo – Institute of Materials Research and Engineering (IMRE), Agency for Science, Technology and Research (A*STAR), Singapore 138634, Singapore; orcid.org/0000-0002-4454-6318

Xiaodong Chen – Innovative Center for Flexible Devices (iFLEX), School of Materials Science and Engineering, Nanyang Technological University, Singapore 639798, Singapore; Institute for Digital Molecular Analytics and Science (IDMxS), Nanyang Technological University, Singapore 636921, Singapore; orcid.org/0000-0002-3312-1664

Xing Sheng – Department of Electronic Engineering, Beijing National Research Center for Information Science and Technology, Center for Flexible Electronics Technology, Tsinghua University, Beijing 100084, China; orcid.org/0000-0002-8744-1700

Complete contact information is available at:
<https://pubs.acs.org/10.1021/acsami.3c08783>

Notes

The authors declare no competing financial interest.

ACKNOWLEDGMENTS

We acknowledge the research scholarship awarded by the Institute of Flexible Electronics Technology of Tsinghua, Zhejiang (IFET-THU), Nanyang Technological University (NTU), and Qiantang Science and Technology Innovation Center, China (QSTIC). This research was financially supported by AcRF Tier-2 grant (MOE2019-T2-2-004), Center of Excellence Grant to Institute for Digital Molecular Analytics and Science (IDMxS) from Singapore Ministry of Education, and the National University of Singapore Presidential Young Professorship Award (22-4974-A0003).

REFERENCES

- (1) Than, A.; Liu, C.; Chang, H.; Duong, P. K.; Cheung, C. M. G.; Xu, C.; Wang, X.; Chen, P. Self-Implantable Double-Layered Micro-Drug-Reservoirs for Efficient and Controlled Ocular Drug Delivery. *Nat. Commun.* **2018**, *9* (1), 4433.
- (2) Wang, Z.; Luan, J.; Seth, A.; Liu, L.; You, M.; Gupta, P.; Rathi, P.; Wang, Y.; Cao, S.; Jiang, Q.; et al. Microneedle Patch for the Ultrasensitive Quantification of Protein Biomarkers in Interstitial Fluid. *Nat. Biomed. Eng.* **2021**, *5* (1), 64–76.
- (3) Than, A.; Liang, K.; Xu, S.; Sun, L.; Duan, H.; Xi, F.; Xu, C.; Chen, P. Transdermal Delivery of Anti-Obesity Compounds to Subcutaneous Adipose Tissue with Polymeric Microneedle Patches. *Small Methods* **2017**, *1* (11), 1700269.
- (4) Zhu, D. D.; Zheng, L. W.; Duong, P. K.; Cheah, R. H.; Liu, X. Y.; Wong, J. R.; Wang, W. J.; Tien Guan, S. T.; Zheng, X. T.; Chen, P. Colorimetric Microneedle Patches for Multiplexed Transdermal Detection of Metabolites. *Biosens. Bioelectron.* **2022**, *212*, 114412.
- (5) Yu, J.; Wang, J.; Zhang, Y.; Chen, G.; Mao, W.; Ye, Y.; Kahkoska, A. R.; Buse, J. B.; Langer, R.; Gu, Z. Glucose-Responsive Insulin Patch

for the Regulation of Blood Glucose in Mice and Minipigs. *Nat. Biomed. Eng.* **2020**, *4* (5), 499–506.

(6) Chang, H.; Zheng, M.; Yu, X.; Than, A.; Seeni, R. Z.; Kang, R.; Tian, J.; Khanh, D. P.; Liu, L.; Chen, P.; et al. A Swellable Microneedle Patch to Rapidly Extract Skin Interstitial Fluid for Timely Metabolic Analysis. *Adv. Mater.* **2017**, *29* (37), 1702243.

(7) Wang, R.; Jiang, X.; Wang, W.; Li, Z. A Microneedle Electrode Array on Flexible Substrate for Long-Term EEG Monitoring. *Sens. Actuators, B* **2017**, *244*, 750–758.

(8) Satti, A. T.; Park, J.; Park, J.; Kim, H.; Cho, S. Fabrication of Parylene-Coated Microneedle Array Electrode for Wearable ECG Device. *Sensors* **2020**, *20* (18), 5183.

(9) Lee, S. J.; Yoon, H. S.; Xuan, X.; Park, J. Y.; Paik, S.-J.; Allen, M. G. A Patch Type Non-Enzymatic Biosensor Based on 3D SUS Micro-Needle Electrode Array for Minimally Invasive Continuous Glucose Monitoring. *Sens. Actuators, B* **2016**, *222*, 1144–1151.

(10) Fattahi, P.; Yang, G.; Kim, G.; Abidian, M. R. A Review of Organic and Inorganic Biomaterials for Neural Interfaces. *Adv. Mater.* **2014**, *26* (12), 1846–1885.

(11) Berggren, M.; Crispin, X.; Fabiano, S.; Jonsson, M. P.; Simon, D. T.; Stavrinidou, E.; Tybrandt, K.; Zozoulenko, I. Ion Electron-Coupled Functionality in Materials and Devices Based on Conjugated Polymers. *Adv. Mater.* **2019**, *31* (22), 1805813.

(12) Liu, Y.; Liu, J.; Chen, S.; Lei, T.; Kim, Y.; Niu, S.; Wang, H.; Wang, X.; Foudeh, A. M.; Tok, J. B.-H.; et al. Soft and Elastic Hydrogel-Based Microelectronics for Localized Low-Voltage Neuro-modulation. *Nat. Biomed. Eng.* **2019**, *3* (1), 58–68.

(13) Kayser, L. V.; Lipomi, D. J. Stretchable Conductive Polymers and Composites Based on PEDOT and PEDOT: PSS. *Adv. Mater.* **2019**, *31* (10), 1806133.

(14) Seeni, R. Z.; Zheng, M.; Lio, D. C. S.; Wiraja, C.; Mohd Yusoff, M. F. B.; Koh, W. T. Y.; Liu, Y.; Goh, B. T.; Xu, C. Targeted Delivery of Anesthetic Agents to Bone Tissues using Conductive Microneedles Enhanced Iontophoresis for Painless Dental Anesthesia. *Adv. Funct. Mater.* **2021**, *31* (47), 2105686.

(15) Yildirim, E.; Wu, G.; Yong, X.; Tan, T. L.; Zhu, Q.; Xu, J.; Ouyang, J.; Wang, J.-S.; Yang, S.-W. A Theoretical Mechanistic Study on Electrical Conductivity Enhancement of DMSO Treated PEDOT: PSS. *J. Mater. Chem. C* **2018**, *6* (19), 5122–5131.

(16) Chen, Y.-H.; De Beeck, M. O.; Vanderheyden, L.; Carrette, E.; Mihajlović, V.; Vanstreels, K.; Grundlehner, B.; Gadeyne, S.; Boon, P.; Van Hoof, C. Soft, Comfortable Polymer Dry Electrodes for High Quality ECG and EEG Recording. *Sensors* **2014**, *14* (12), 23758–23780.

(17) Jing-Qi, S.; Xi-Zheng, Z.; LIANG, C.-Y.; Zi-Xu, Y.; Yan, L.; Dian-Peng, Q. The Monitoring of Plant Physiology and Ecology: from Materials to Flexible Devices. *Chin. J. Anal. Chem.* **2022**, *51*, 100211.

(18) Degli Agosti, R. Touch-Induced Action Potentials in Arabidopsis Thaliana. *Arch. Sci.* **2014**, *67*, 125–138.

(19) Liu, Y.; Feig, V. R.; Bao, Z. Conjugated Polymer for Implantable Electronics toward Clinical Application. *Adv. Healthcare Mater.* **2021**, *10* (17), 2001916.

(20) Mombrú, D.; Romero, M.; Faccio, R.; Mombrú, A. W. Raman Microscopy Insights on the out-of-Plane Electrical Transport of Carbon Nanotube-Doped PEDOT: PSS Electrodes for Solar Cell Applications. *J. Phys. Chem. B* **2018**, *122* (9), 2694–2701.

(21) Liu, S.; Deng, H.; Zhao, Y.; Ren, S.; Fu, Q. The Optimization of Thermoelectric Properties in a PEDOT: PSS Thin Film through Post-Treatment. *RSC Adv.* **2015**, *5* (3), 1910–1917.

(22) Chou, T.-R.; Chen, S.-H.; Chiang, Y.-T.; Lin, Y.-T.; Chao, C.-Y. Highly Conductive PEDOT: PSS Films by Post-Treatment with Dimethyl Sulfoxide for ITO-Free Liquid Crystal Display. *J. Mater. Chem. C* **2015**, *3* (15), 3760–3766.

(23) Hosseini, E.; Kollath, V. O.; Karan, K. The Key Mechanism of Conductivity in PEDOT: PSS Thin Films Exposed by Anomalous Conduction Behaviour upon Solvent-Doping and Sulfuric Acid Post-Treatment. *J. Mater. Chem. C* **2020**, *8* (12), 3982–3990.

(24) Luo, Y.; Li, W.; Lin, Q.; Zhang, F.; He, K.; Yang, D.; Loh, X. J.; Chen, X. A Morphable Ionic Electrode Based on Thermogel for Non-

Invasive Hairy Plant Electrophysiology. *Adv. Mater.* **2021**, *33* (14), 2007848.

(25) Gibson, L. J. The Hierarchical Structure and Mechanics of Plant Materials. *J. R. Soc., Interface* **2012**, *9* (76), 2749–2766.

(26) Fromm, J.; Lautner, S. Electrical Signals and Their Physiological Significance in Plants. *Plant Cell Environ.* **2007**, *30* (3), 249–257.

(27) Sukhova, E.; Sukhov, V. Electrical Signals, Plant Tolerance to Actions of Stressors, and Programmed Cell Death: Is Interaction Possible? *Plants* **2021**, *10* (8), 1704.

(28) Vodeneev, V.; Akinchits, E.; Sukhov, V. Variation Potential in Higher Plants: Mechanisms of Generation and Propagation. *Plant Signal. Behav.* **2015**, *10* (9), No. e1057365.

(29) Blyth, M. G.; Morris, R. J. Shear-Enhanced Dispersion of a Wound Substance as a Candidate Mechanism for Variation Potential Transmission. *Front. Plant Sci.* **2019**, *10*, 1393.

(30) Kumari, A.; Chételat, A.; Nguyen, C. T.; Farmer, E. E. Arabidopsis H⁺-ATPase AHA1 Controls Slow Wave Potential Duration and Wound-Response Jasmonate Pathway Activation. *Proc. Natl. Acad. Sci. U.S.A.* **2019**, *116* (40), 20226–20231.

(31) Gallé, A.; Lautner, S.; Flexas, J.; Fromm, J. Environmental Stimuli and Physiological Responses: The Current View on Electrical Signalling. *Environ. Exp. Bot.* **2015**, *114*, 15–21.

(32) Sukhov, V.; Akinchits, E.; Katicheva, L.; Vodeneev, V. Simulation of Variation Potential in Higher Plant Cells. *J. Membr. Biol.* **2013**, *246*, 287–296.

(33) White, P. J.; Broadley, M. R. Calcium in Plants. *Ann. Bot.* **2003**, *92* (4), 487–511.

(34) Yoon, C.-Y.; Noh, J.; Lee, J.; Kee, Y. K.; Seo, C.; Lee, M.; Cha, M.-U.; Kim, H.; Park, S.; Yun, H.-R.; et al. High and Low Sodium Intakes Are Associated with Incident Chronic Kidney Disease in Patients with Normal Renal Function and Hypertension. *Kidney Int.* **2018**, *93* (4), 921–931.

(35) Grillo, A.; Salvi, L.; Coruzzi, P.; Salvi, P.; Parati, G. Sodium Intake and Hypertension. *Nutrients* **2019**, *11* (9), 1970.

(36) Kader, M. A.; Lindberg, S. Cytosolic Calcium and pH Signaling in Plants under Salinity Stress. *Plant Signal. Behav.* **2010**, *5* (3), 233–238.

(37) Hatsugai, N.; Katagiri, F. Quantification of Plant Cell Death by Electrolyte Leakage Assay. *Bio-Protoc.* **2018**, *8* (5), No. e2758.

(38) Qiu, L.; Wang, Y.; Qu, H. Loading Calcium Fluorescent Probes into Protoplasts to Detect Calcium in the Flesh Tissue Cells of *Malus domestica*. *Hortic. Res.* **2020**, *7*, 91.

(39) Hush, J.; Overall, R.; Newman, I. A Calcium Influx Precedes Organogenesis in *Graptopetalum*. *Plant Cell Environ.* **1991**, *14* (7), 657–665.

(40) Gao, W.; Emaminejad, S.; Nyein, H. Y. Y.; Challa, S.; Chen, K.; Peck, A.; Fahad, H. M.; Ota, H.; Shiraki, H.; Kiriya, D.; et al. Fully Integrated Wearable Sensor Arrays for Multiplexed in situ Perspiration Analysis. *Nature* **2016**, *529* (7587), 509–514.

Recommended by ACS

Bilingual Bidirectional Stretchable Self-Healing Neuristors with Proprioception

Rui Qiu, Min Zhang, *et al.*

JUNE 29, 2023
ACS NANO

READ 

Biodegradable Microelectrodes for Monitoring the Dynamics of Extracellular Ca²⁺ in Rat Brain

Huiming Wang, Meining Zhang, *et al.*

MAY 22, 2023
ANALYTICAL CHEMISTRY

READ 

Inkjet-Printed Polyelectrolyte Seed Layer-Based, Customizable, Transparent, Ultrathin Gold Electrodes and Facile Implementation of Photothermal Effect

Duhee Kim, Hongki Kang, *et al.*

APRIL 11, 2023
ACS APPLIED MATERIALS & INTERFACES

READ 

Nanoneedle-Electrode Devices for *In Vivo* Recording of Extracellular Action Potentials

Tomoaki Banno, Takeshi Kawano, *et al.*

JULY 05, 2022
ACS NANO

READ 

Get More Suggestions >

Supporting Information

Dual-Conductive and Stiffness-Morphing Microneedle Patch Enables Continuous in Planta Monitoring of Electrophysiological Signal and Ion Fluctuation

Lingxuan Kong^a, Hanqi Wen^{a,b}, Yifei Luo^c, Xiaodong Chen^{d,e}, Xing Sheng^f, Yuxin
Liu^{c,g,h,i,*}, Peng Chen^{a,e,*}

*^aSchool of Chemistry, Chemical Engineering and Biotechnology, Nanyang
Technological University, 637457, Singapore*

*^bInstitute of Flexible Electronics Technology of THU, Jiaxing, Zhejiang 314000,
China*

*^cInstitute of Materials Research and Engineering (IMRE), Agency for Science,
Technology and Research (A*STAR), 2 Fusionopolis Way, 138634, Singapore*

*^dInnovative Center for Flexible Devices (iFLEX), School of Materials Science and
Engineering, Nanyang Technological University, 50 Nanyang Avenue, 639798
Singapore*

*^eInstitute for Digital Molecular Analytics and Science (IDMxS), Nanyang
Technological University, 636921, Singapore*

^fDepartment of Electronic Engineering, Beijing National Research Center for Information Science and Technology, Center for Flexible Electronics Technology, Tsinghua University, 100084, China

^gDepartment of Biomedical Engineering, College of Design and Engineering, 4 Engineering Drive 3, National University of Singapore, 117583, Singapore

^hInstitute for Health Innovation & Technology iHealthtech, National University of Singapore, 117599, Singapore

ⁱThe N.1 Institute for Health, National University of Singapore, 117456, Singapore

Corresponding Author

*Yuxin Liu (lyx@nus.edu.sg); +65 65660182

*Peng Chen (ChenPeng@ntu.edu.sg); +65 65141086

Table of Contents

Figure S1 Fabrication of DSMNP	4
Figure S2 SEM Image of DSMNP	4
Figure S3 EIS of DSMNP	5
Figure S4 EDS analysis of DSMNP	6
Figure S5 Mechanical compression test of DSMNP before and after penetration	6
Figure S6 Area-specific impedance (ASI, at 10 Hz) of DSMNP change after penetration	7
Figure S7 Resistant variation when different bending angle being applied	8
Figure S8 EIS fitting of DSMNP- and Ag wire-leaf interface	8
Figure S9 EIS of DSMNP- and Ag wire-agarose interface with model fitting	9
Figure S10 FTIR spectra of pristine PEDOT:PSS and DMSO-doped PEDOT:PSS	10
Figure S11 Wind-induced motion artifact root-mean-square (RMS) of DSMNP and Ag wire.	11
Figure S12 Comparison of variation potentials induced by flame-burning and mechanical wounding	12
Table S1 Cell constants for DSMNP conductivity calculation	13
Table S2 EIS fitting parameters of DSMNP	14
Table S3 EIS fitting parameters of DSMNP- and Ag wire-leaf interfaces	14
Table S4 EIS fitting parameters of DSMNP- and Ag wire-agarose interfaces ...	15

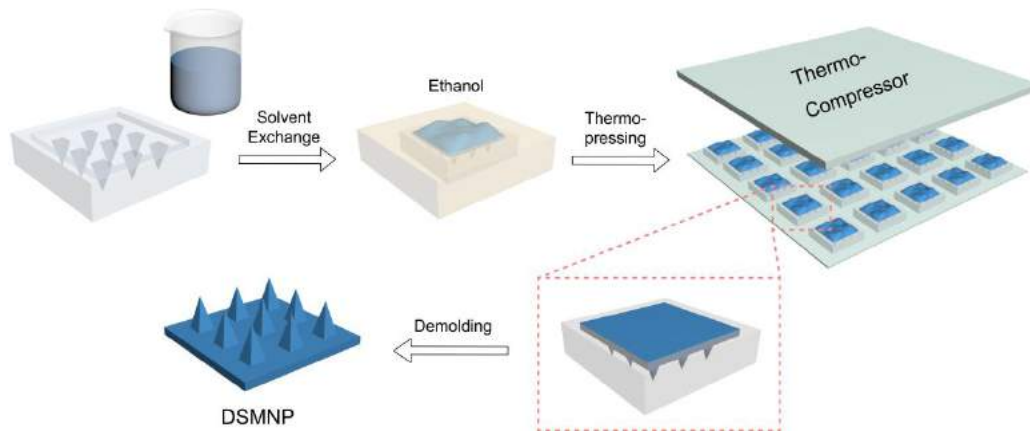


Figure S1. Fabrication of DSMNP.

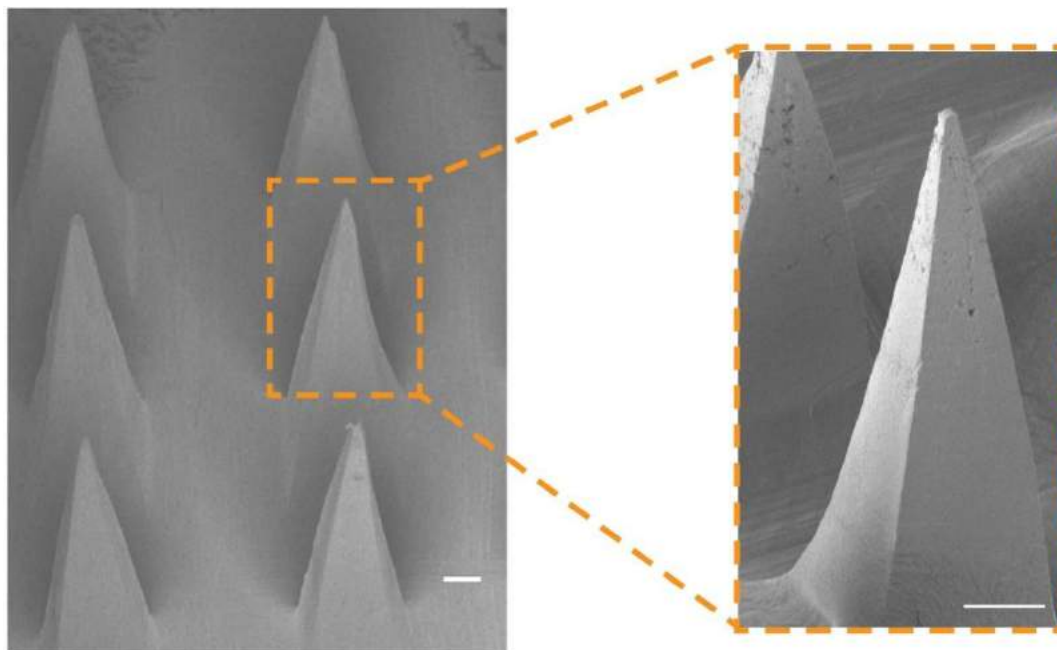


Figure S2. SEM image of DSMNP. Scale bar: 100 μm .

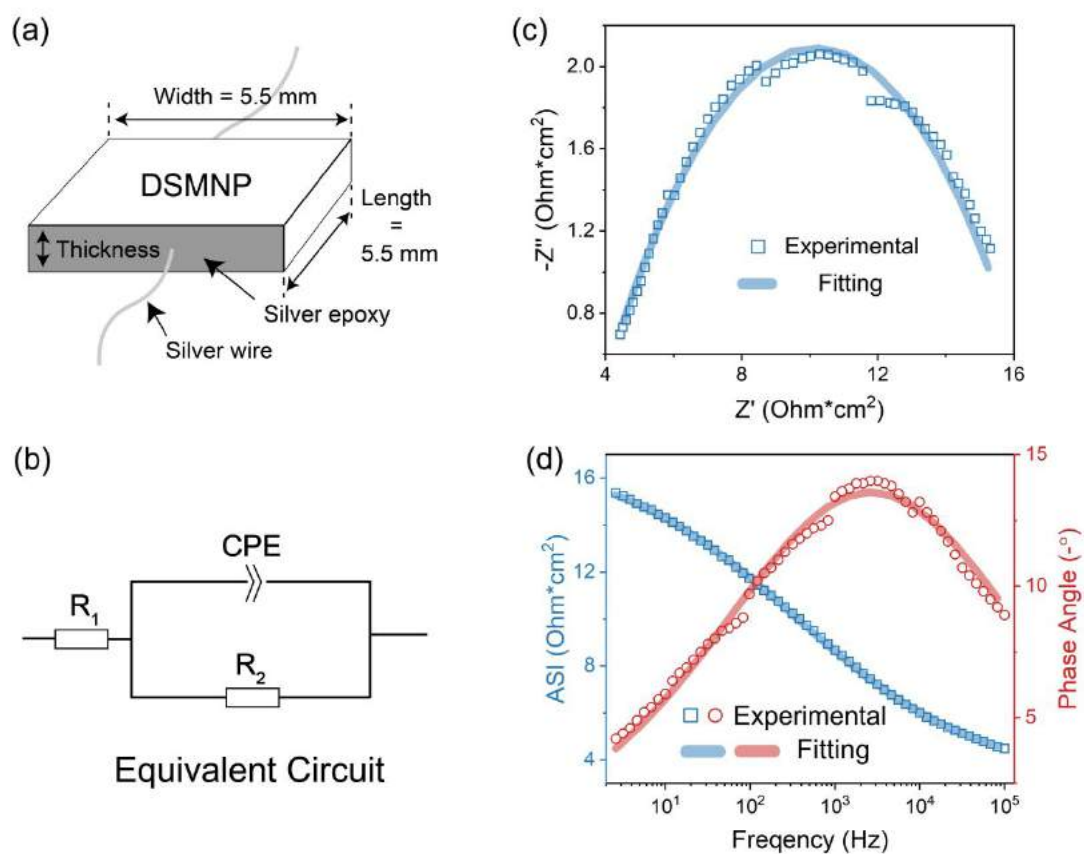


Figure S3. EIS of DSMNP. (a) Experimental set-up for impedance measurement. (b) Equivalent circuit for data fitting (R_1 : wire resistance and contact resistance; R_2 : equivalent resistance of DSMNP; CPE: constant phase element of DSMNP). (c) Nyquist plot of DSMNP (experimental and fitting data). (d) Bode plot of DSMNP (experimental and fitting data).

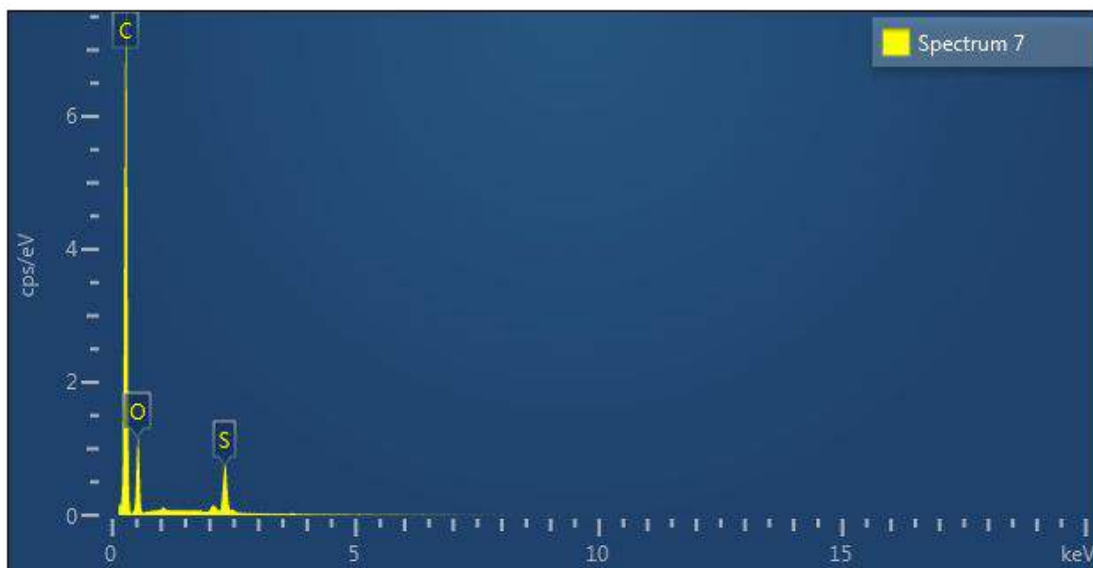


Figure S4. EDS analysis of DSMNP.

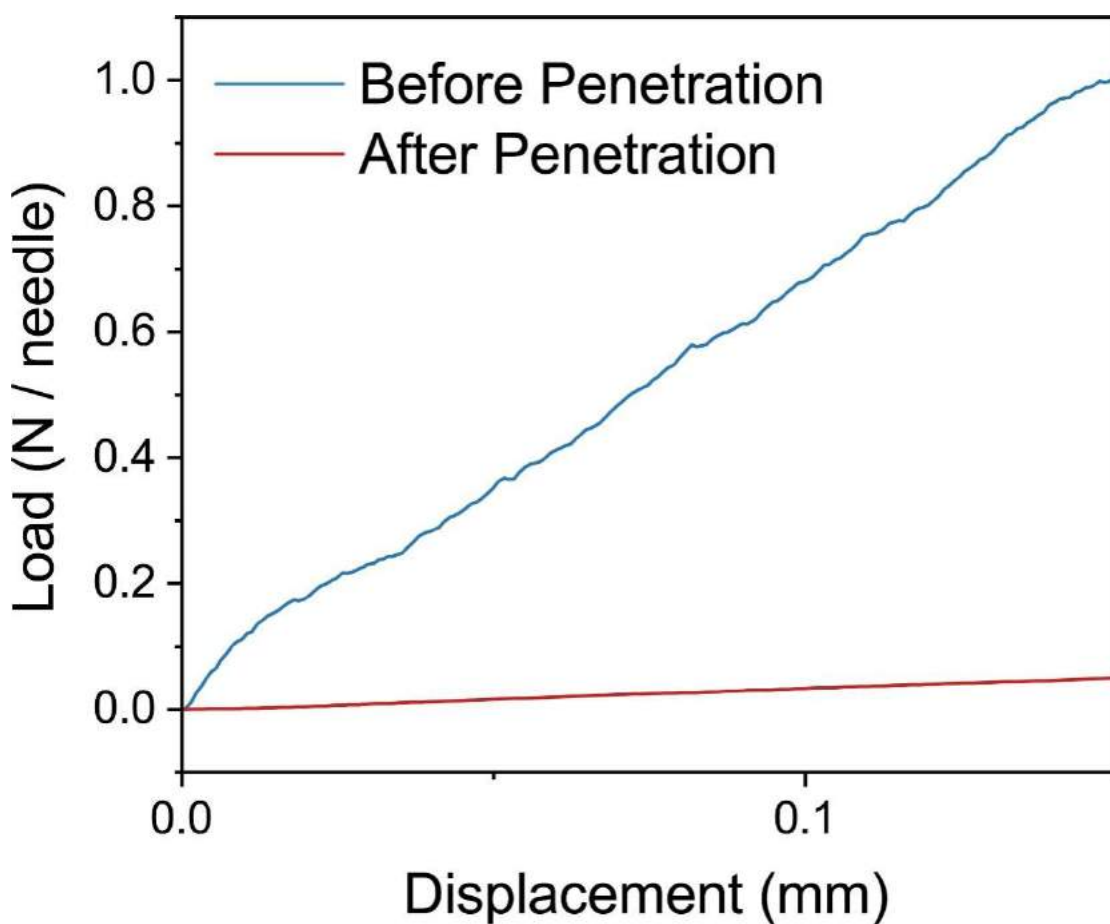


Figure S5. Mechanical compression test of DSMNP before and after penetration.

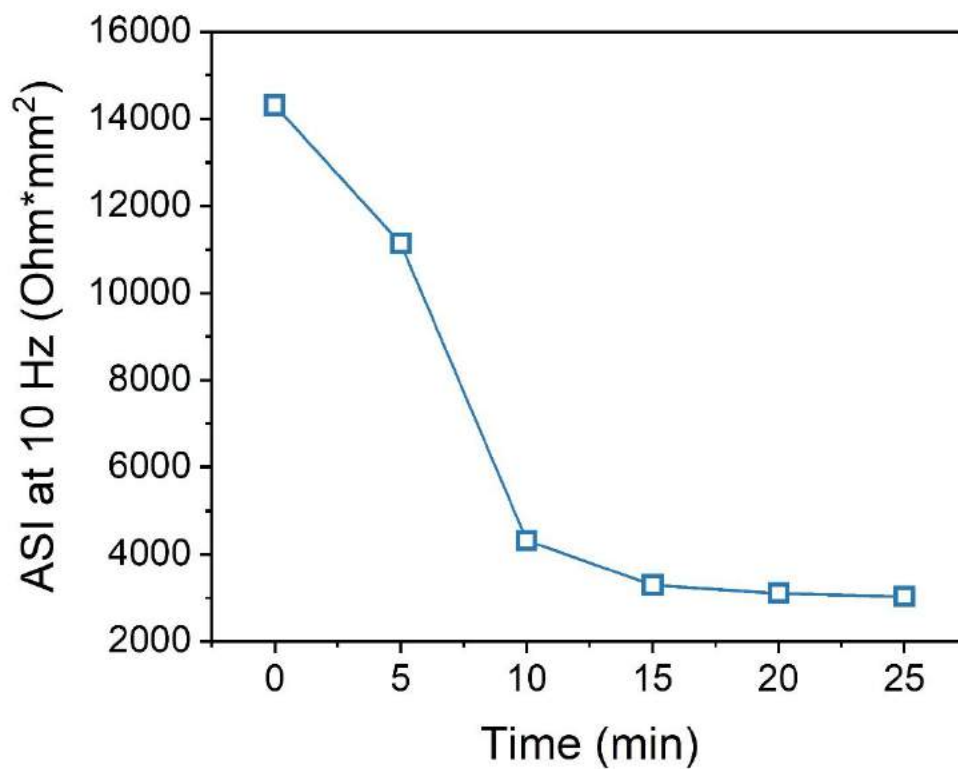


Figure S6. Area-specific impedance (ASI, at 10 Hz) of DSMNP change after penetration.

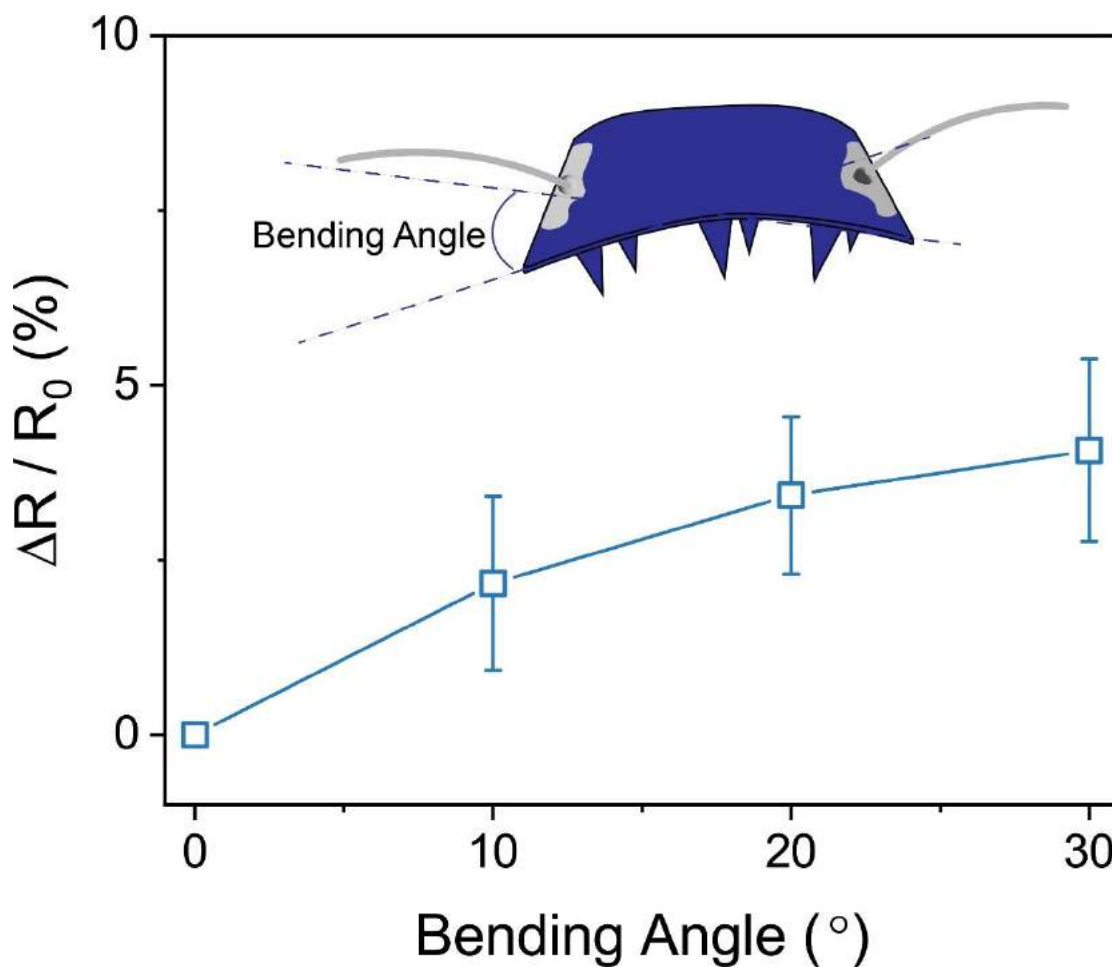


Figure S7. Resistant variation when different bending angle being applied (Inset: experiment set-up for bending angle measurement).

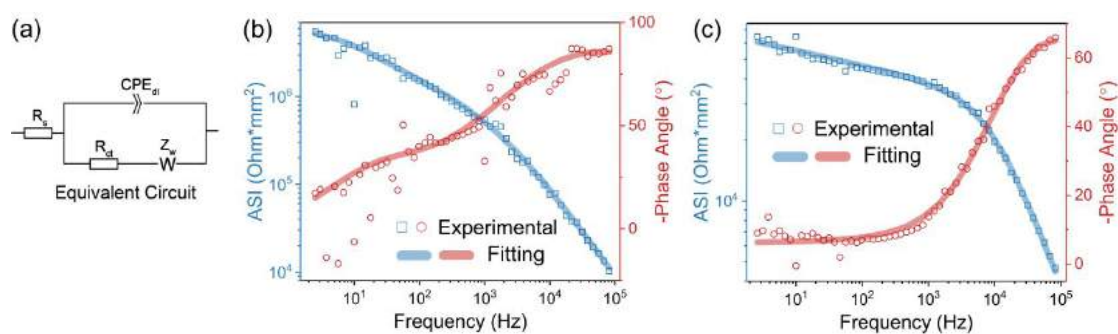


Figure S8. EIS fitting of Ag wire- and DSMNP-leaf interface. (a) Equivalent circuit for EIS fitting (Randles circuit model). (b) Fitting of EIS experimental data of Ag wire-leaf interface. (c) Fitting of EIS experimental

data of DSMNP-leaf interface.

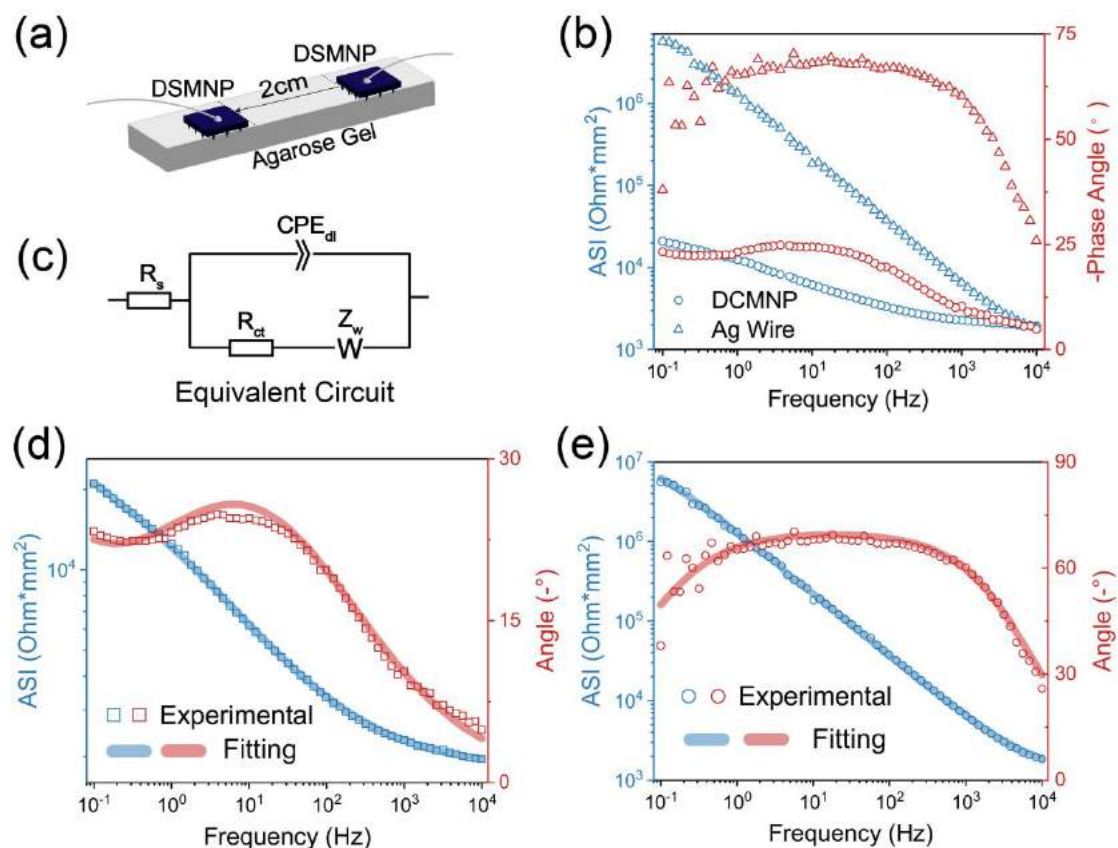


Figure S9. EIS of DSMNP- and Ag wire-agarose interface with model fitting. Agarose gel (4% agar + 96% phosphate buffer solution to mimic biological tissue containing interstitial fluid) was covered with a water-impermeable parafilm (mimicking stratum corneum in human skin or plant cuticle). (a) Experimental set-up. (b) Area-specific impedance (ASI) spectra (left) and phase angle (right) of Ag wire- and DSMNP-agarose interface. Inset: illustration of the experiment setup. (c) Equivalent circuit for EIS fitting (Randles circuit model). (d) Fitting of EIS experimental data of DSMNP-agarose interface. (e) Fitting of EIS experimental data of Ag wire-agarose interface.

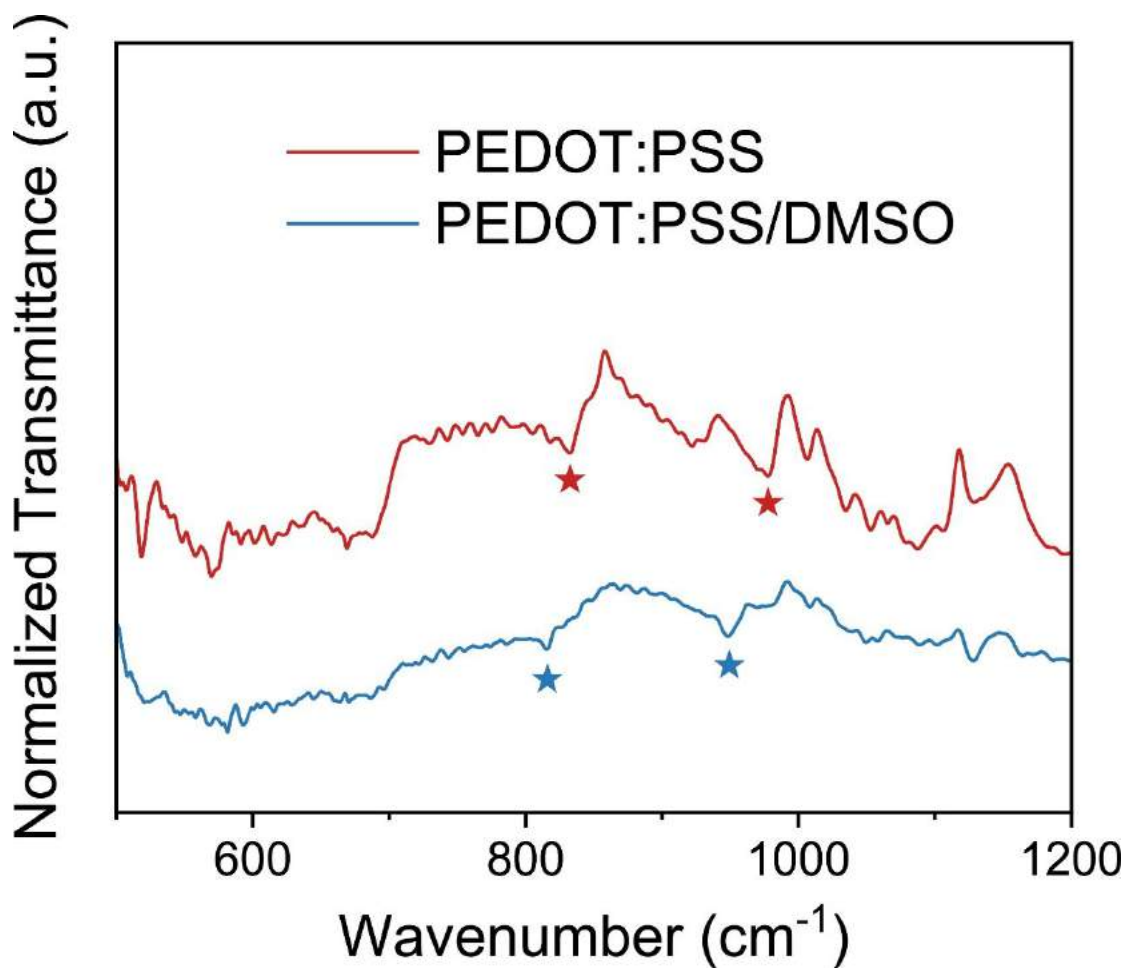


Figure S10. FTIR spectra of pristine PEDOT:PSS and DMSO-doped PEDOT:PSS.

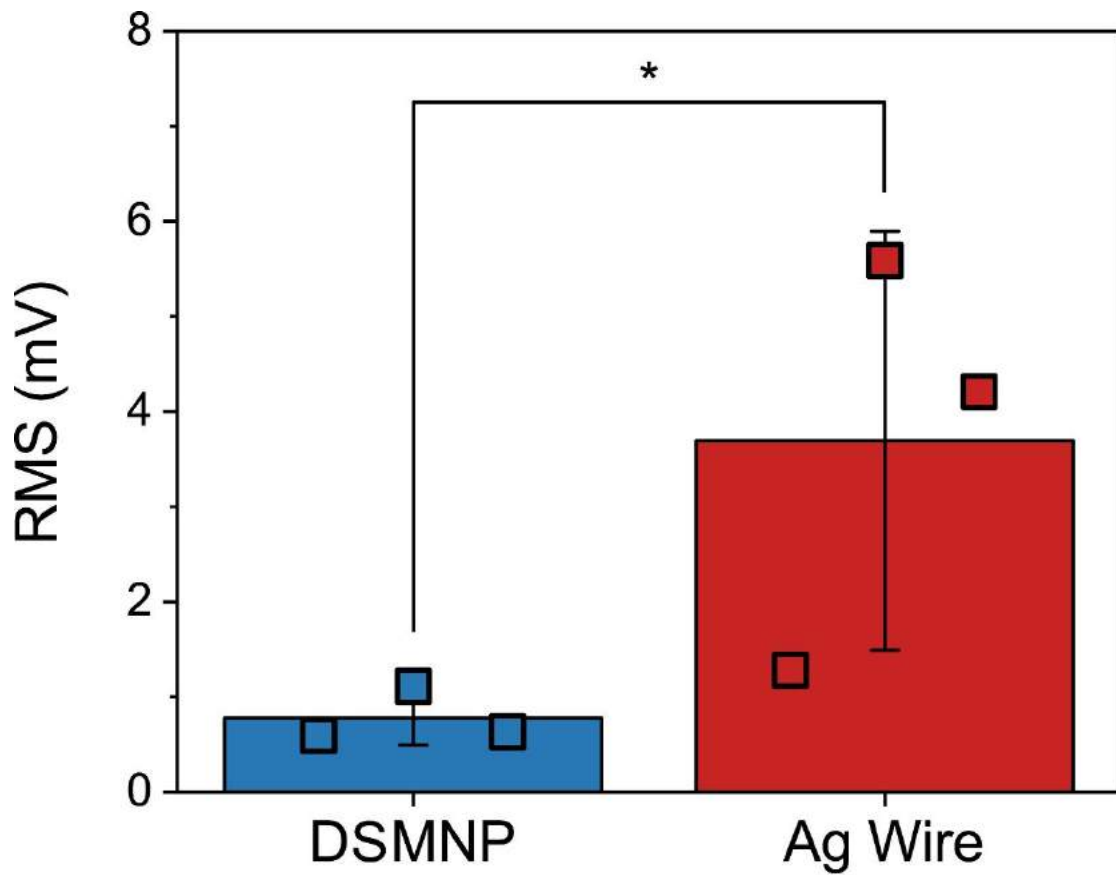


Figure S11. Wind-induced motion artifact root-mean-square (RMS) of DSMNP and Ag wire. Unpaired, two tailed t-test ($n = 3$) was used for statistical analysis. $P = 0.08544$; $*P < 0.1$.

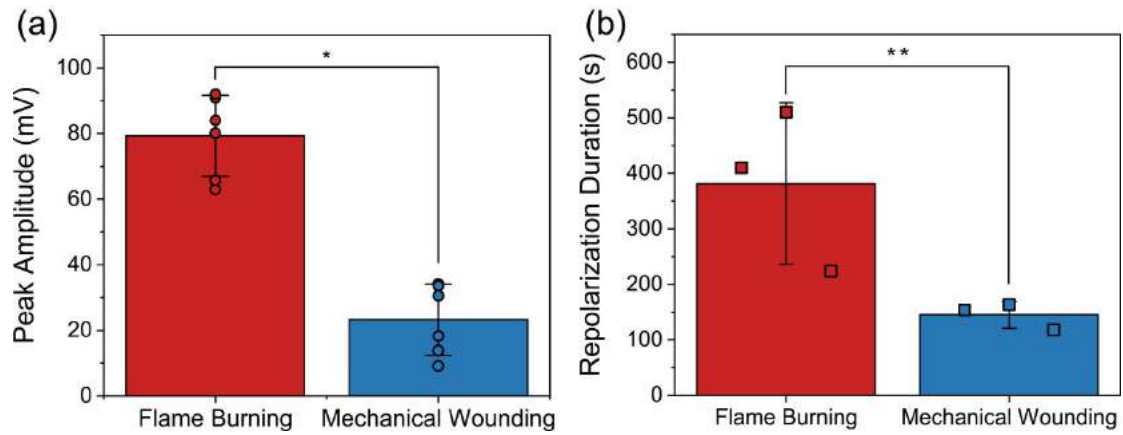


Figure S12. Comparison of variation potentials induced by flame-burning and mechanical wounding. (a) Amplitude comparison. Unpaired, two tailed t-test ($n = 6$) was used for statistical analysis. $P = 8.33487 \cdot 10^{-6}$; $*P < 0.05$. (b) Repolarization duration comparison (till stabilization). Unpaired, two tailed t-test ($n = 3$) was used for statistical analysis. $P = 0.05002$; $**P < 0.1$.

Table S1. Cell constant for DSMNP conductivity calculation.

PEDOT:PSS Concentration (wt%)	Cell Constant (cm ⁻¹)	Average (cm ⁻¹)	Standard Deviation (cm ⁻¹)
15	23.256	31.677	10.870
	24.390		
	43.478		
	25		
	47.619		
	26.316		
20	58.824	40.192	12.858
	52.632		
	38.462		
	25.641		
	32.258		
	33.333		
25	41.667	42.188	12.370
	37.037		
	32.258		
	37.037		
	66.667		
	38.462		

30	41.667	56.227	16.033
	43.478		
	76.923		
	62.5		
	71.429		
	41.667		

Table S2. EIS fitting parameters of DSMNP.

R_1 (Ω cm ²)	Y_0 (10^{-3} S s ⁿ cm ⁻²)	n	R_2 (Ω cm ²)
3.2025	4.48368	0.37166	13.9125

Table S3. EIS fitting parameters of DSMNP- and Ag wire-leaf interfaces.

Sample	R_s (Ω mm ²)	Y_0 (10^{-9} S s ⁿ mm ⁻²)	n	R_{ct} (Ω mm ²)	Z_w (10^{-7} S s ^{1/2} mm ²)
DSMNP- leaf interface	802.5	3.945	0.827	12452	2.279
Ag Wire- leaf interface	730.9	0.3175	0.953	777590	0.03055

Table S4. EIS fitting parameters of DSMNP- and Ag wire-agarose interfaces.

Sample	R_s ($\Omega \text{ cm}^2$)	Y_0 ($10^{-7} \text{ S s}^n \text{ cm}^{-2}$)	n	R_{ct} ($\Omega \text{ cm}^2$)	Z_w ($10^{-7} \text{ S s}^{1/2} \text{ cm}^2$)
DSMNP- agarose interface	778.7	579.1	0.8	9697	289.2
Ag Wire- agarose interface	1026	2.256	0.7824	$1.161 \cdot 10^7$	8.468